RESEARCH ARTICLE

NANO · MICRO small
www.small-journal.com

Structural Control Enables Catalytic and Electrocatalytic Activity of Porous Tetrametallic Nanorods

Dániel Zámbó, Dávid Kovács, GyörgyZ. Radnóczi, Zsolt E. Horváth, Attila Sulyok, István Tolnai, and András Deák*

Integrating more than one type of metal into a nanoparticle that has a well-defined morphology and composition expands the functionalities of nanocatalysts. For a metal core/porous multimetallic shell nanoparticle, the availability of catalytically active surface sites and molecular mass transport can be enhanced, and the multielemental synergy can facilitate intraparticle charge transport. In this work, a reliable and robust synthesis of such a functional tetrametallic nanoparticle type is presented, where a micro- and mesoporous PdPtIr shell is grown on Au nanorods. The effect of critical synthesis parameters, namely temperature and the addition of HCl are investigated on the hydrodynamic size of the micellar pore template as well as on the stability of the metal chloride complexes and various elemental analysis techniques prove composition of the porous multimetallic shell. Due to the synergistic properties, the tetrametallic nanorods possess extensive negative surface charge making them a promising catalyst in reduction reactions. Dye degradation as well as the conversion of p-nitrophenol to p-aminophenol is catalyzed by the supportless nanorods without light illumination. By depositing the particles onto conductive substrates, the nanostructured electrodes show promising electrocatalytic activity in ethanol oxidation reaction. The nanocatalyst presents excellent morphological stability during all the catalytic test reactions.

1. Introduction

Noble metal nanoparticles, in general, have been in the focus of the catalysis-related research due to their finely controllable shape, size, surface chemistry and physicochemical properties endowing them with enhanced catalytic activity. Moreover, precise control over the composition and structural properties of these particles has enabled the bridging of homogeneous and heterogeneous catalysis: the existence of highly available active sites are combined with the possibility of separation, purification and recycling.[1] A vast library of catalytic applications of monometallic noble metal nanoparticles have been explored including Ag, Au, Pt, Pd, Ir, Rh, Ru with well-controlled shapes in numerous catalytic and electrocatalytic reactions.[2] Among these noble metals, Pt can be considered as a benchmark catalyst due to its intrinsic activity especially for oxygen reduction reaction (ORR) and hydrogen evolution reaction (HER), which is unapproachable by earth-abundant metals.[3] Nevertheless, Pt-based catalysts often suffer from sluggish kinetics, significant overpotential and unsatisfactory stability hindering their widespread application in future fuel cells.[4] It has been revealed in the last decade that the performance of supported monometallic nanoparticle-based catalysts lags behind their multimetallic counterparts. Thus, combining two or more metals into well-defined nanoparticles paved the way towards advanced applications and enhanced overall performance.[5] Introducing a second or third metal in the synthesis of metal nanoparticles expands their properties and functionalities, however, the structure and morphology were found to play an important role in their catalytic performance.[5,6] In recent years, different combinations of noble metals such as Au-Pt,[7] Au-Pd,[8] Pd-Pt,[9,10] Pt-Ir[11] and Au-Pd-Pt[12–14] in forms of nanoalloys or core-shell particles have been intensively studied including the impact of the morphology and composition on their performance. Although the random and ordered intermetallic alloying of metals are promising strategies for improving the catalytic activity of noble metal nanoparticles, superiority of core-shell structures was demonstrated for the combination of Au and Pt.[15]

Besides compositional control, precise synthesis of porous metal nanocrystal catalysts[16] further expanded the functionalities (stability, mass and electron transfer, electronic effects)[17] and performance of mono- and multimetallic nanocrystals in (electro)catalysis.[18–23] Syntheses of such nanoparticles with

D. Zámbó, D. Kovács, G. Radnóczi, Z. E. Horváth, A. Sulyok, I. Tolnai, A. Deák
HUN-REN Centre for Energy Research
Konkoly-Thege M. út 29–33, Budapest H-1121, Hungary
E-mail: daniel.zambo@ek.hun-ren.hu
D. Kovács
Department of Physical Chemistry and Materials Science, Faculty of Chemical Technology and Biotechnology
Budapest University of Technology and Economics
Műegyetem rkp. 3, Budapest H-1111, Hungary

The ORCID identification number(s) for the author(s) of this article can be found under https://doi.org/10.1002/smll.202400421

DOI: 10.1002/smll.202400421

greatly enhanced availability of surface sites mostly involve the use of a template. This can be a mesoporous silica template[24] or a pore-forming agent (e.g., PEO-PPO-PEO or PEO-PMMA block copolymers) followed by the layer-by-layer like deposition of the additional metals.[13,21,25,26] Multielemental synergy combined with the high porosity is of extreme advantage in multimetallic nanoparticles, due to the novel electronic properties boosting their electrocatalytic activity.[19] Concerning porous noble metal nanoparticles, synergy between Au, Pd, Pt and Ir enabled the enhancement of Pt's properties in terms of mass activity and durability. Using Pd is an excellent approach to alter the electronic properties of Pt via shifting the position of its d-band center being in close correlation with the adsorption strength and catalytic activity of the metal sites,[27] leading to better electrooxidation properties. Similarly, incorporation of Ir in Pt-based catalyst also downshifts the d-band center of Pt, resulting in enhanced resistance against CO poisoning[28] and also the catalytic oxidation of H_2O_2 was found to be enhanced.[29] The shape of the multimetallic nanoparticle catalysts[30] as well as the location of the different metals are of great importance in optimizing their (electro)catalytic performance.[31,32] For Au and Pd, Hosseini et al. showed an improved activity of bimetallic catalyst on TiO_2 support during volatile organic compounds (VOCs) oxidation, when the core consisted of Au and the shell was made of Pd (compared to the opposite and alloyed structures).[33] Consequently, synthesizing an Au core-multimetallic shell structure is a promising strategy to enhance the catalytic properties. Considering the additional advantages of Ir NPs in sensing[34] and catalytic reduction of nitroaromatic compounds,[35] exploiting the multielemental synergy in Au@PdPtIr system might extend the range of applications even further. However, while synthetic approaches and application of bi- and trimetallic nanoparticles have been already reported in many papers, tetrametallic nanoparticles are significantly less explored in the literature.

The wet-chemical preparation of multimetallic nanoparticles requires the simultaneous reduction of different ionic species, but the complex reduction reaction of the combination of metal salts is not fully understood yet. Especially for porous multimetallic particles the co-reduction of two or more metals is a challenging task due to the fact that their reduction cannot be simply predicted by the standard potentials and it is greatly influenced by the reducing agent, pore-forming additives and the coordination environment.[19] Additionally, the pore forming agent might also take part in the reaction, hence, its effect on the growth kinetics must also be taken into account. The synergy between the metals within a well-defined nanoparticle manifests in the altered electronic properties compared to those of their monometallic counterparts. Combining Au, Pd and Pt enables the emergence of novel electronic properties by promoting the charge transfer from the core metal to the shell metals.[12] In the background of this effect, the difference of the Fermi levels (i.e., contact potential)[36] as well as the lattice strain upon growth onto the Au core can be anticipated.[37] Gold does not only enhance the catalytic activity of Pd, but it also increases the durability of the catalysts and eases the removal of intermediates.[38,39] Advantages of Au@PdPtIr porous multimetallic nanoparticles would also include the high availability of the active sites of the small metal grains beside accelerating the mass transport due to the large specific surface area of the shell. Pt nanograins in the size range of 2–5 nm were found to show outstanding activity in alcohol electrooxidation reactions,[40–43] hence, combining electronic properties as a result of multielemental synergy, porous core-shell morphology and the fine structure of the shell endow the tetrametallic nanoparticles with excellent multifunctionality.

In this paper, a robust and reliable synthetic method for the preparation of tetrametallic, Au@PdPtIr nanorods with a micro- and mesoporous trimetallic shell is reported. The technical aspects of the synthesis including the temperature-dependent micelle size of the pore forming copolymer as well as the effect of the acid during the growth are discussed in-detail. In the first step, a porous shell of Pd and Pt is formed on Au nanorods followed by the decoration of the shell's outer surface with Ir particles. The optimized protocol provides tetrametallic nanorods in a short time and in high concentration. Structural properties and compositional analysis revealed the fine structure of the tetrametallic nanorods consisting of small metal nanograins (≈3.7 nm) in the shell. Electrophoretic mobility measurements shed light on the intrinsic charge transport within the particles and indicate excessive negative charge on their outer surface. Due to the unique electronic property, the highly available surface sites, and the multielemental synergy, the particles are found to be (electro)catalytically active in multiple test reactions. Organic dye (methylene blue) can be effectively degraded in the presence of Au@mPdPtIr particles in dark conditions without external light illumination. Conversion of p-nitrophenol to p-aminophenol can also be achieved in the dark. When the particles are deposited on conductive substrate, they are active in ethanol electrooxidation reaction as well. Importantly, the synthesized multifunctional catalyst particles preserve their original morphology in all investigated catalytic reactions, which confirms their durable structure and composition in catalytic reactions.

2. Results and Discussion

2.1. Synthesis and Characterization of The Nanoparticles

Anisometric micro- and mesoporous multimetallic nanoparticles (mNRs) were synthesized using Au nanorods (AuNRs, length: 74 ± 7 nm, width: 17 ± 1 nm) as seeds followed by the wet-chemical reduction of three noble metals (Pd, Pt and Ir) in two subsequent steps. For the preparation of the nanorod seeds, the robust and precisely tunable synthesis[44,] using CTAB and sodium oleate was employed, resulting in AuNRs with high shape and size purity (Figure S1, Supporting Information). After the removal of the unreacted species and concentration of the AuNRs in 50 mM CTAB, the seed solution's shelf life can be extended to at least 6 months. The reduction of the additional metals in a form of a porous shell was carried out in two steps but one pot: Pd^{2+}, Pt^{2+} and Pt^{4+} ions were reduced in the presence of F127 copolymer micelles and ascorbic acid at 70 °C, followed by the decoration of the mesoporous shell with Ir domains using ascorbic acid and $NaBH_4$ reducing agents at 80 °C. The deposition of the PdPt mesoporous shell and its subsequent decoration with Ir take place in a heat block within 40 and 20 minutes, respectively, without using ultrasonication. Pluronic F127 serves as a template in the shell growth process resulting in micro- and mesoporous AuR@mPtPdIr nanorods with highly available surface

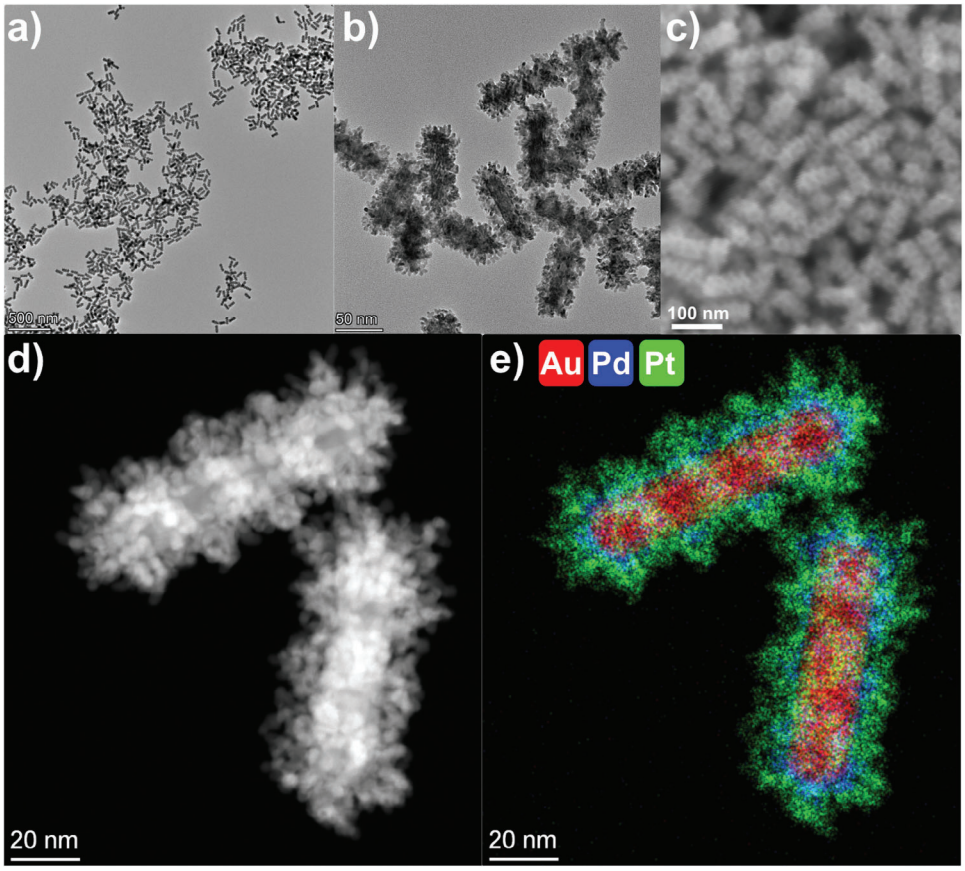

Figure 1. TEM a,b), SEM c), HAADF d) images and elemental maps of the synthesized mesoporous tetrametallic nanorods e). Note: iridium cannot be reliably visualized due to its low amount and the spectral overlapping with Pt.

sites. **Figure 1** shows the morphology of the particles with dimensions of 102 ± 7 nm (in length) and 44 ± 3 nm (in width) possessing micropores and mesopores with the diameter of 1.2 ± 0.3 nm and 13 ± 2 nm, respectively (Figure S1d,e, Supporting Information). The shell thickness was found to be ca. 15 nm. Elemental mapping proves that first a porous Pd layer forms around the AuNR seeds surrounded by a thicker and highly porous Pt shell consisting of small Pt nanoparticles (3.7 ± 0.5 nm, Figure S1c, Supporting Information). Reduction of iridium is challenging due to the stability of Ir(III),[45] and its strong coordination with Cl^-,[46] thus, the preparation of ultrasmall metallic iridium domains without overoxidation to IrO_x requires a strong reducing agent.[34,35,47] Hence, Ir was deposited on the AuR@mPdPt particles in a second step using ascorbic acid and $NaBH_4$ simultaneously. Visualization of Ir in the TEM-EDX maps is cumbersome, due to the relatively low Ir content of the particles and its spectral overlapping with Pt being present in higher concentration (Figure 1e), nevertheless, the elemental maps confirm the layer-like deposition of Pd and Pt with their preferential location around the AuNRs. High resolution images revealing the crystal lattice of the particles show a nearly uniform lattice orientation over the entire particle. Small deviations can be seen, these are most probably caused by bending after growth. This means that growth on the Au seed took place epitaxially resulting in nearly uniformly oriented (face centered cubic) yet porous layers around the seed (see Figure S2, Supporting Information for details).

The optimized protocol provides AuR@mPdPtIr nanorods with outstanding shape and size purity (Figure S3, Supporting Information).

The particles show extensive scattering and prominent extinction in the UV-Vis-NIR wavelength range (**Figure 2A**) mostly in the UV (< 400 nm) and NIR regions (900 – 1400 nm). The former can be associated with the presence of small Pd, Pt and Ir particles, while the latter is the residual longitudinal dipolar resonance of the AuNRs. Tetrametallic nanorods show quasi-constant absorption in the visible wavelength range (pure absorption spectrum without scattering can be seen in Figure S4, Supporting Information). XRD patterns of tetrametallic nanorods, and as a reference, the pristine gold nanorods, are presented in Figure 2b. Powder Diffraction File (PDF) cards 04–0784 (Gold), 04–0802 (Platinum) and 46–1043 (Palladium) were used to identify the XRD peaks. All the three metals have face-centered cubic (Fm-3m) crystallographic structure with different lattice parameters. (111), (200) and (220) lines of Au, Pt and Pd phases expected in the measured range are denoted by orange, red, and green bars, respectively. Peak positions of the pristine AuNR reference sample coincide with the Au line positions and corresponding peaks are present in the XRD plot of the tetrametallic nanorods, too. Considering the positions of the Pt and Pd lines, the peaks at

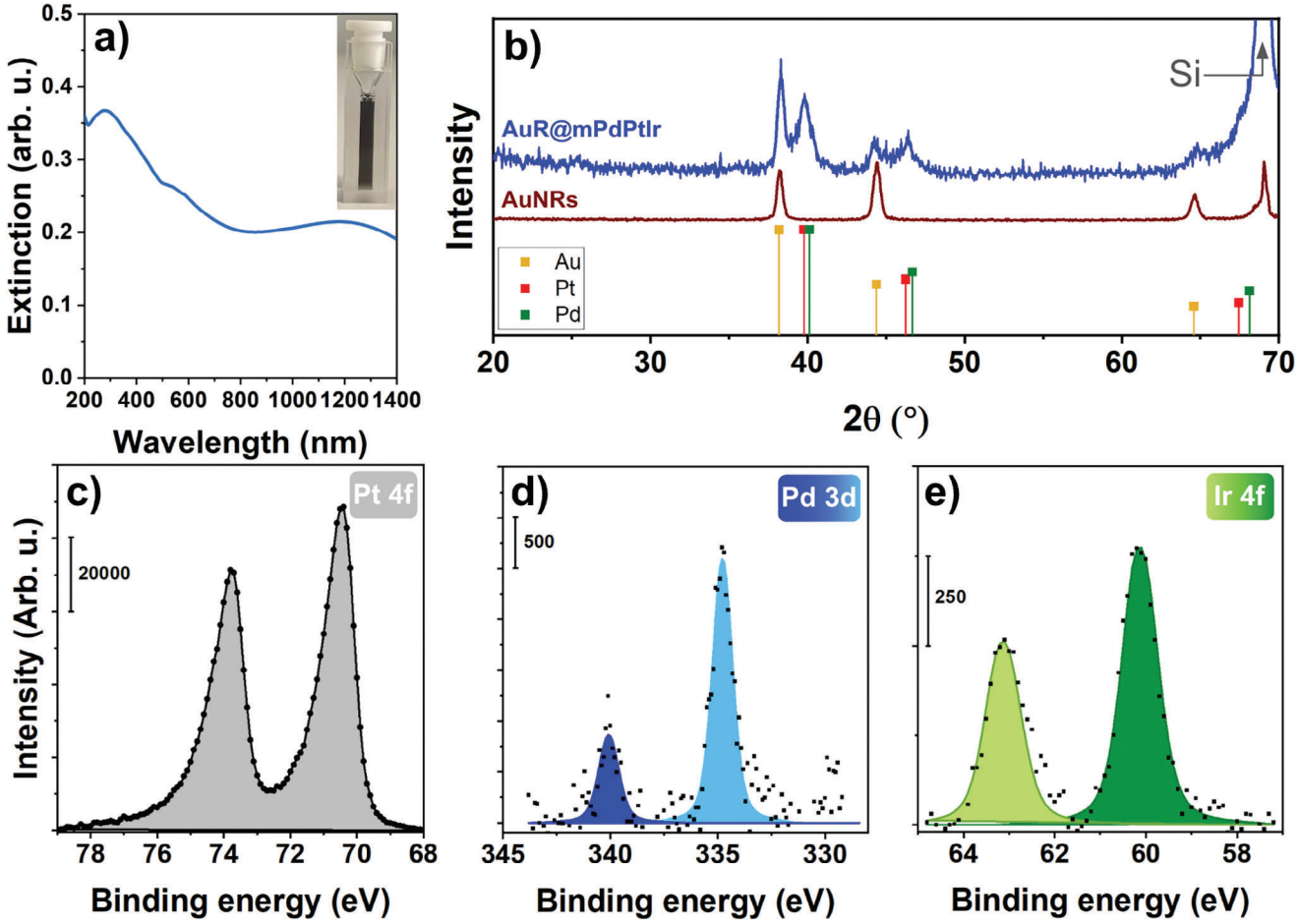

Figure 2. UV-Vis-NIR extinction spectrum of the tetrametallic nanorods a). XRD diffractogram b) of the multimetallic nanorods and the pristine Au nanorods used as core particles. XPS peaks of the detectable metals in their relevant binding energy ranges: Pt 4f c), Pd 3d d) and Ir 4f e). Inset of panel (a) shows the color of the mesoporous nanorod solution.

$2\Theta = 39.7°$ and $2\Theta = 46.4°$ can be identified as overlapping Pt and Pd (111) and (200) peaks, respectively, while the (220) peak expected at about $2 = 67.5°$ is overspread by the intensive (400) peak of the single crystalline silicon sample holder. Nevertheless, X-ray diffraction pattern also supports the presence of Au, Pd and Pt in the tetrametallic nanorods.

Both electron microscopy and X-ray-based techniques fail to detect the low amounts of Ir in the presence of Pt due to their small difference in d-spacing and spectral overlap, thus, other analytical techniques were employed to determine the Ir content of the AuR@mPdPtIr particles. Figure 2c–e show the XPS spectra of the detectable elements, namely Pt, Pd and Ir. The measured peaks of platinum are centered at 70.45 eV ($4f_{7/2}$) and 73.80 eV ($4f_{5/2}$). Palladium shows peaks at 334.81 eV ($3d_{5/2}$) and 340.11 eV ($3d_{3/2}$), while the peaks of iridium can be found at 60.14 eV ($4f_{7/2}$) and 63.11 eV ($4f_{5/2}$). These values agree well with the nominal ones of the metallic Pt, Pd and Ir. Due to the layered nature of the mesoporous shell, Au cannot be detected owing to the limited mean path of the photoelectrons. Palladium can be reached by the photoelectrons which is attributed to the porous structure of the shell. The outer surface of the mNRs consists of Pt and Ir. Importantly, Ir was also found to be in metallic form (Ir^0, Figure 2e) just like for Pd and Pt.

To determine the exact composition of the tetrametallic nanorods, SEM-EDX and ICP-OES analyses were performed by depositing mNRs on silicon wafer and after digesting the particles in aqua regia, respectively. **Table 1** summarizes the quantitative analysis of the particles and the total metal concentration of the mNR stock solution. The presence of Ir is proven by the ICP-OES analysis and the Pt/Ir molar ratio was found to be 159.26. It has to be noted that XPS also provided the Pt/Ir atomic ratio (146.3), which is in line with the ICP results further confirming that the Ir locates at the outer region of the porous shell.

Tetrametallic nanorods have well-defined pores in their shells (Figure 1b), which can be attributed to the presence of F127 copolymer in the form of micelles during the shell deposition. When using a templating surfactant in such systems, temperature and polymer concentration have a crucial impact on the size and structure of the micelles which is often overlooked. **Figure 3** shows the dynamic light scattering (DLS) size distribution of F127 micelles as a function of concentration and temperature. At room temperature (25 °C), F127 forms micellar structures with bimodal distribution at higher concentrations which gradually

Table 1. Elemental composition of tetrametallic nanorods measured by SEM-EDX and ICP-OES and the derived molar ratios of metal pairs.

Analysis technique	Unit	Au	Pd	Pt	Ir	Total metal conc.	molar ratios of metal pairs			
							Au/Pd	Pt/Pd	Pt/Au	Pt/Ir
SEM-EDX	at%	24.70	19.89	55.41	n/A	–	1.24	2.79	2.25	*n/A*
ICP-OES	ppm	544.69	242.04	1196.98	7.41	1991.11	1.22	2.70	2.22	157.33
	mmol/L	2.765	2.274	6.136	0.039	11.21				

turns monomodal with smaller hydrodynamic sizes (<10 nm) for lower concentrations. However, increasing the temperature causes a pronounced shift in the size of the micelles towards larger hydrodynamic diameters. Monomodal distributions with smaller polydispersity indices can be achieved in a wide concentration range by increasing the temperature to 70 °C. At this temperature, average hydrodynamic sizes of 20–28 nm can be obtained in the 0.05 – 5 wt% concentration range (Figure 3c). Moreover, higher temperature also facilitates the reduction of metal salts, thus, the synthesis can be performed within an hour in total.

During the optimization of the synthetic protocol, the role of HCl was found to be crucial for the reproducibility as well as shape and size purity of the multimetallic nanorods. In the absence of HCl, or by adding the HCl after mixing the metal precursors and F127 solution the yield of the mNR synthesis decreases dramatically. In these conditions, significant homogeneous nucleation occurs, which deteriorates the deposition of the multimetallic shell onto the gold nanorods. To shed light on the origin of this observation, the effect of HCl and F127 on the optical properties of the metal precursor solutions was investigated. While the optical spectrum of Pt^{2+}, Pt^{4+} and Ir^{3+} solutions remain unchanged when adding different volumes of HCl (without adding F127), a gradual change in the spectrum of the Pd^{2+} solution can be observed (**Figure** 4a–d). This spectral shift can be attributed to the gradual transition of $PdCl_3(H_2O)^-$ complex to $[PdCl_4]_2^-$ as a function of the increasing Cl^- concentration.[48,49] It indicates, that HCl plays an important role to provide the $[PdCl_4]_2^-$ complex for the Pd deposition. Moreover, evolution of the spectrum of the Pd^{2+} precursor solution in the presence of F127 in the absence of HCl was also monitored in a 30 minute interval (Figure 4e). The solution almost immediately turns brownish after the addition of F127 and the extinction of the band at 425 nm gradually increases in 10 minutes. This indicates the formation of Pd nanoparticles in the solution, which is also confirmed by TEM (Figure 4f). However, when the F127 solution is first mixed with HCl followed by the injection of the Pd precursor, the spectrum changes only slightly in the time period of 120 minutes (Figure S5, Supporting Information). This implies, that F127 itself is able to reduce the palladium precursor solution in the absence of HCl resulting in homogeneously nucleated Pd particles serving as seeds for the further growth of the mesoporous shell in the AuR@mPdPtIr synthesis (Figure S6, Supporting Information). This is in agreement with the recent findings of Sokolsay-Papkov et al., who reported on the template-assisted synthesis of Au nanoparticles using Pluronic F127.[50] At pH = 2.2, the reduction of the Au precursor was significantly slowed down, while increasing the pH of the solution led to the formation of AuNPs as a results of the decomposition of F127.[50] Consequently, adding HCl before the injection of the metal precursors in the presence of F127 is of extreme importance to ensure the reliability and robustness of the tetrametallic nanorods' synthesis. After clarifying the above-mentioned aspects of the synthesis, porous anisometric tetrametallic nanorods in high concentration can be prepared in a robust and reliable manner within an hour without the need of ultrasonication (detailed procedure can be found in the Experimental Section).

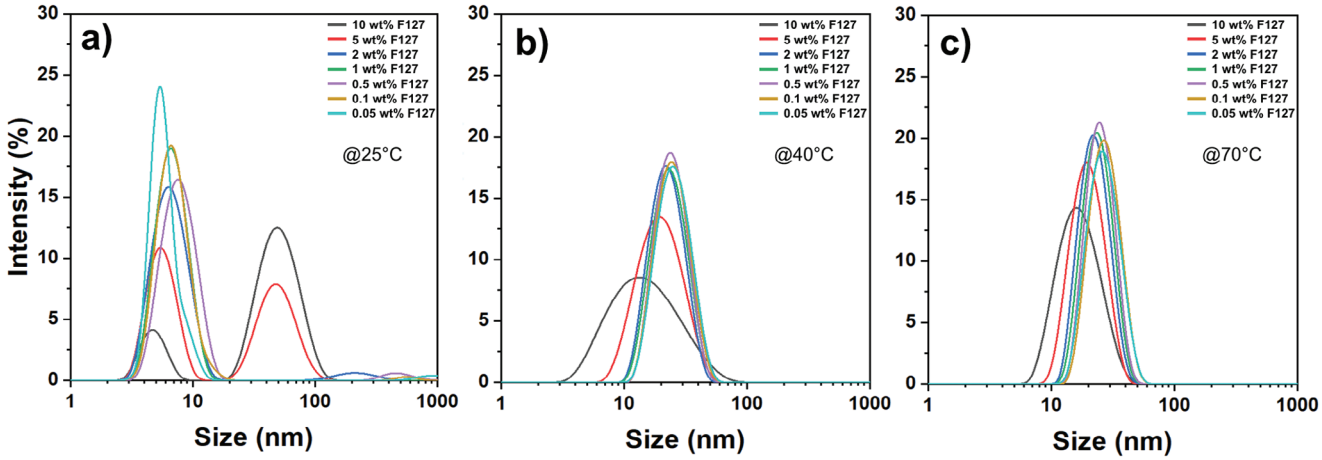

Figure 3. Effect of the temperature (25 °C a), 40 °C b), and 70 °C c) on the F127 micelle size distribution measured by dynamic light scattering for different copolymer concentrations.

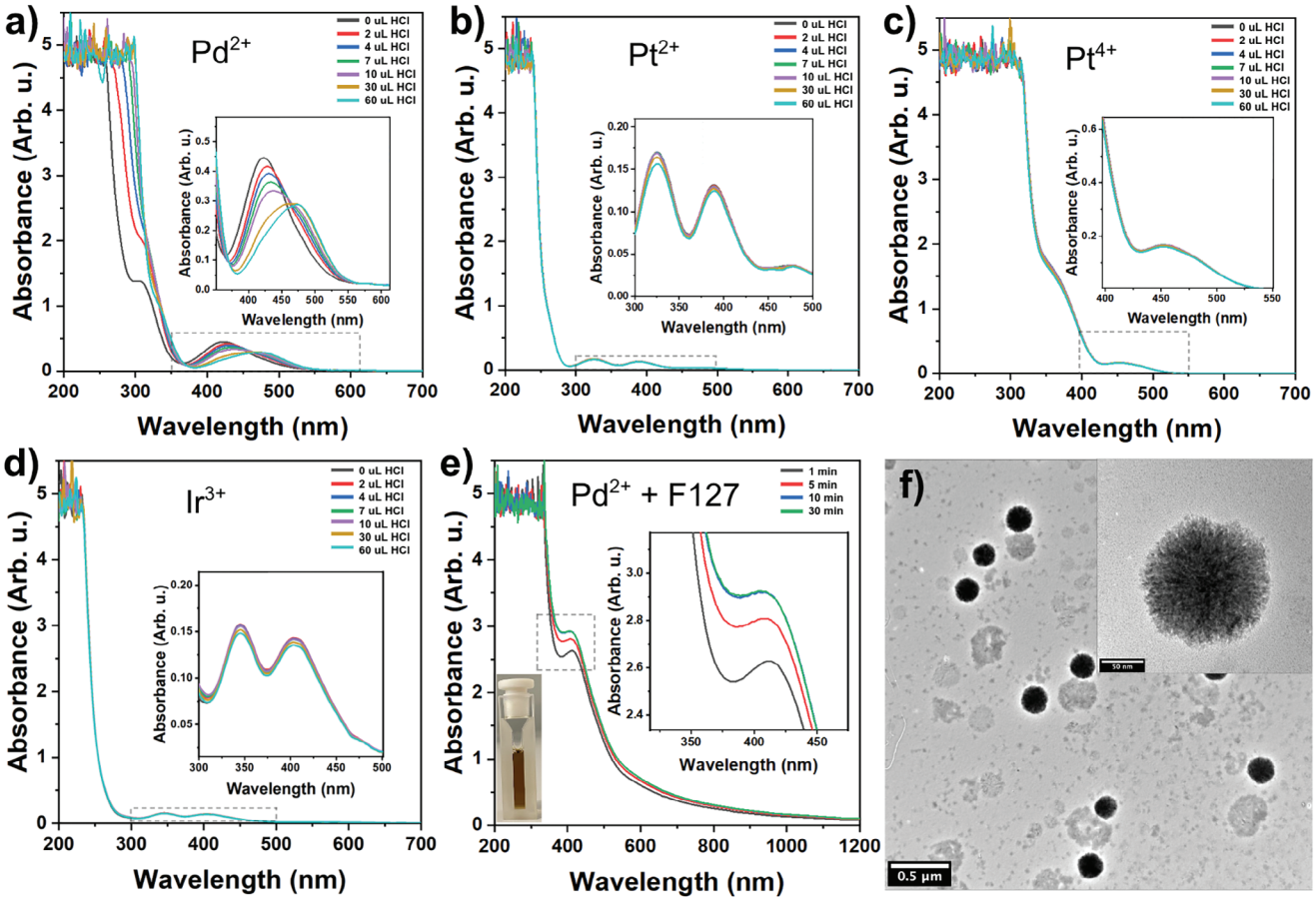

Figure 4. Effect of the HCl concentration on the UV-Vis spectra of Pd^{2+} a), Pt^{2+} b), Pt^{4+} c), and Ir^{3+} d) solutions. Time evolution of the spectrum of Pd^{2+} solution in the presence of F127 without added HCl e). TEM image of Pd nanoparticles formed upon the addition of F127 solution in the absence of HCl f).

2.2. Ligand-Free Tetrametallic Nanorods Possess Highly Negatively Charged Surface

After the synthesis and extensive purification of the tetrametallic nanorods, unreacted species and excess of F127 were removed from the mNR solution. Measuring the electrophoretic mobility of the particles revealed that mNRs possess extensive negative surface charge (electrophoretic mobility is of −2.94 µmcm Vs^{-1}, see Figure S7a, Supporting Information). To rule out the effect of any residual F127 or complex ions on the electrophoretic mobility, the particles were further washed with MilliQ water in 4 additional centrifugation/redispersion cycles. After this treatment, the particles can be considered quasi ligand-free. Importantly, particles preserve their negative electrophoretic mobility being −3.07 ± 0.35 µmcm Vs^{-1} as average (Figure S7b, Supporting Information). Considering that the deposition of the trimetallic shell was performed onto the surface of positively charged AuNRs (EM = + 1.02 ± 0.09 µmcm Vs^{-1}, NRs dispersed in F127 with residual CTAB on their surface), the obtained negative electrophoretic mobility is a consequence of the shell growth itself, as F127 is a neutral copolymer with no charges. Hence, this can be attributed to the synergistic interplay between the applied noble metals altering the electronic properties of the tetrametallic nanorods and facilitating the charge transfer from the Au core towards the trimetallic shell. Consequently, it can be anticipated that the tetrametallic nanorods' catalytic and electrocatalytic performance are enhanced due to the higher binding affinity of the adsorbates towards the mNRs' surface sites.

2.3. Application of the Tetrametallic Nanorods in Catalytic Reactions

2.3.1. Conversion of p-nitrophenol to p-aminophenol

Catalytic properties of porous tetrametallic nanorods were first tested in dark conditions to convert p-nitrophenolate to p-aminophenolate. First, p-nitrophenol stock solution was diluted to 0.08 mM and 0.16 mM in a quartz cuvette, and 0.1 M $NaBH_4$ was added to prepare the analyte (p-nitrophenolate anion). After injecting the mNR stock, the reaction was monitored by UV–vis spectroscopy to follow the conversion of p-nitrophenolate (at the wavelength of 400 nm) to p-aminophenolate (at 299 nm) in time. **Figure** 5a shows the evolution of the UV–vis spectrum in the course of 60 minutes in a typical experiment. After

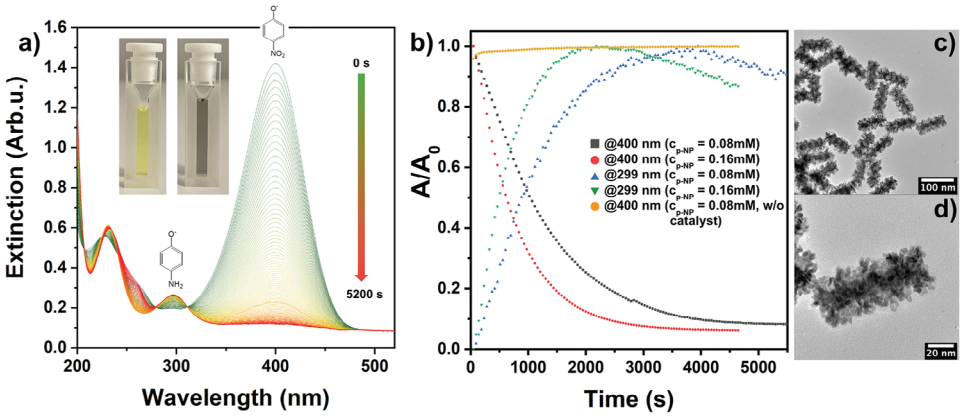

Figure 5. Temporal evolution of the UV–vis spectra of p-nitrophenol in the presence of multimetallic nanorods in dark conditions a). Kinetics of the p-nitrophenol to p-aminophenol transformation measured at the main peaks of the corresponding compounds b). TEM images of the catalyst nanorods after the reaction c,d). Inset of panel (a) shows the color of the p-nitrophenolate and the solution after the catalytic reaction.

extracting the extinction values at 400 and 299 nm, the kinetics of the conversion can be revealed (Figure 5b). Using the present catalyst, 98.95 % and 99.95 % of p-nitrophenolate (for $8•10^{-5}$ M and $1.6•10^{-5}$ M, respectively) can be removed from the solution (Figure S8a, Supporting Information). Without the catalyst, p-nitrophenolate remains stable in the solution, while mNRs facilitated the complete conversion in 60 minutes.

The reduction of p-nitrophenol most likely follows the established mechanism[51] involving BH_4^- anions as hydride source and the multimetallic nanorod catalyst as electron transfer agent. Upon the hydrolysis of sodium borohydride, the deprotonation of p-nitrophenol to p-nitrophenolate anion occurs imparting a prominent yellow color to the solution, which gradually vanishes in time in the presence of the catalyst indicating the reduction of the p-nitrophenolate anion to p-aminophenol.

After fitting the decay of the extinction at 400 nm with a pseudo first-order kinetics equation, rate constants for the two investigated p-nitrophenolate concentrations were found to be similar (Figure S9, Supporting Information), indicating that the reaction is diffusion-limited. It is important to emphasize that the porous nanorods preserve their morphology and porosity in the catalytic conversion, hence neither the shape of the nanorods nor their fine structure change and they retain their colloidal stability as well (Figure 5c,d). This implies that the nanorods indeed serve as a heterogeneous catalyst in the process, moreover, the electron transport between the catalyst and the analyte (with the aid of $NaBH_4$) takes place without any external trigger.

The tetrametallic nanorods can be easily separated from the reaction solution and are able to catalyze the reduction of p-nitrophenol in three consecutive cycles with a minimal decrease in the final degradation value (Figure S10a, Supporting Information).

2.3.2. Degradation of Methylene Blue in Dark Conditions

Electrophoretic mobility measurements revealed that the mNRs possess negative surface charge, which makes them a promising candidate for removing organic pollutants. To test their performance in a prototypical dye degradation reaction, positively charged methylene blue was chosen as an analyte to degrade in the presence of the nanorods in dark conditions. Temporal spectral changes in methylene blue solution were monitored in the presence of mNRs in a fiber-coupled visible spectrometer for 5700 s with 5 seconds temporal resolution. **Figure 6a** shows the time-dependent spectra, clearly indicating the degradation of the methylene blue (peak centered around 663 nm). In the catalytic process, 92.49 % of the added methylene blue can be degraded (Figure S8b, Supporting Information). The extinction decay at the peak maximum over time was used to highlight the kinetics of the degradation (black solid curve in Figure 6b). Sequential addition of the same amount of methylene blue but in 9 subsequent portions supported the determination of the rate constant of the reaction's pseudo first-order kinetics (see Figure S11, Supporting Information and the related table). To exclude any eventual impact of the continuous illumination by the spectrometer lamp on the degradation process during the time-dependent spectroscopic measurements, control experiments were carried out by illuminating the solution with a high-power, UV-filtered Xe lamp for the same period of time at spectroscopic measurement performed at discrete time instances (red dots in Figure 6b). The reaction was also performed under the complete exclusion of light and a single measurement performed at the end of the reaction (magenta triangle in Figure 6b). It can be inferred that the reaction is also completed in fully dark conditions, and Xe-illumination did not change the kinetics, verifying that the system is insensitive to the light and the catalytic activity is not due to any photogenerated charge carrier. Naturally, in the absence of the catalyst, methylene blue was stable in the course of time. While recent studies report on the catalytic degradation of methylene blue in the presence of trimetallic nanoparticles,[52,53] it has to be emphasized that in the presence of our tetrametallic nanorods neither light nor $NaBH_4$ are necessary to degrade the dye.

To shed light on the possible mechanism of the dye degradation, experiments in the presence of different scavengers were performed. Sodium sulfate, 2-propanol and p-benzoquinone were employed as O_2, $OH^{\cdot}$ and $O_2^{-\cdot}$ scavengers, respectively.

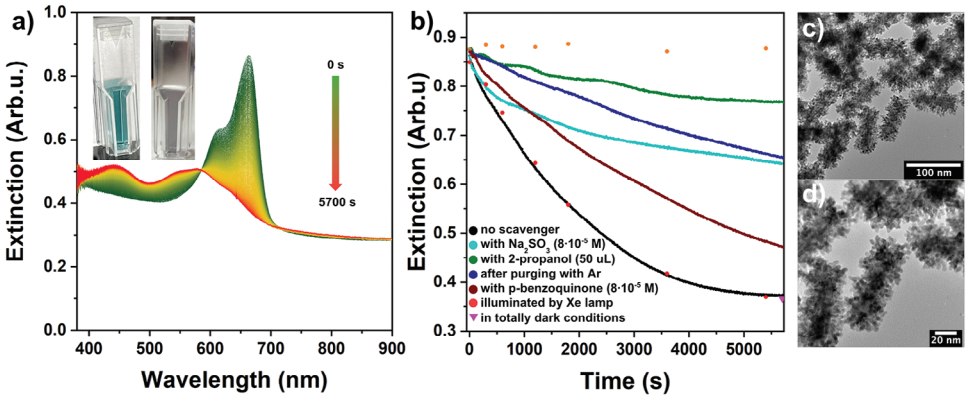

Figure 6. Temporal evolution of the visible spectra of methylene blue in the presence of multimetallic nanorods in dark conditions a). Inset shows the photographs of the sample before and at the end of the reaction. Kinetics of the dye degradation measured at 663 nm in the absence of catalyst, in the presence of catalyst and by adding different scavengers b). TEM images of the catalyst nanorods after the methylene blue degradation reaction c,d) in the absence of scavengers.

Furthermore, the methylene solution was bubbled with Ar for 15 minutes before the introduction of mNRs to decrease the concentration of dissolved O_2. While all scavengers significantly slowed down the rate of the dye degradation reaction, 2-propanol was found to be the most efficient scavenger to hinder the reaction. Dissolved O_2 and superoxide radicals are responsible for the generation of H_2O_2 which can further produce OH radicals indirectly,[54] introduction of 2-propanol directly suppresses the OH radical concentration. Hence, $OH^{\cdot}$ radical was found to be the responsible reactant for the degradation of methylene blue catalyzing the N-demethylation of the dye and decomposing it to smaller aromatic compounds. After performing the dye degradation reaction, the mNRs were found to be intact: nanorods preserved their size, shape, fine structure and colloidal stability (Figure 6c,d). It has to be noted, that the degradation of methylene blue produces degradation products, which are present in the UV-Vis spectrum after the catalytic reaction (Figure S12, Supporting Information). These reaction products are most likely smaller aromatic compounds (produced via N-demethylation of MB)[55] such as aminocatechol and aminobenzothiazol derivatives[56] being present in the solution after removing the catalyst by centrifugation. Similarly for p-nitrophenol reduction, methylene blue can also be efficiently degraded in three consecutive recycling of the nanorod catalyst (Figure S10b, Supporting Information).

2.3.3. Electrocatalytic Oxidation of Ethanol in Alkaline Medium

Multimetallic nanoparticles are of great interest in direct fuel cell application, thus, electrocatalytic reactions have been in the focus of the test reactions for this material class. Therefore, we investigated the electrocatalytic activity of mNRs in ethanol oxidation reaction (EOR) in alkaline medium. Electrodes were fabricated from the nanorods by depositing the concentrated particle "ink" in a rectangular mold on MPTMS-functionalized ITO glass (see Experimental section for details). Mass activity of the electrodes was investigated as a function of the ink volume as well as the scan rate of the cyclic voltammetry measurement in a conventional three-electrode electrochemical cell using the mNRs@ITO as the working electrode. While MPTMS-functionalized ITO is inactive in EOR (Figure S13, Supporting Information), tetrametallic nanorods show pronounced activity in electrocatalytic oxidation of ethanol: a main peak in the anodic scan indicates the oxidation of ethanol to acetaldehyde and acetic acid, whilst the sharp peak in the cathodic scan can be attributed to the oxidation of freshly diffusing alcohols (**Figure 7**).[57,58] The latter peak is intensive and sharp, which implies that the oxidation of the metals in the catalyst particles is not prominent. Nonetheless, scan rate was found to have an impact on the overpotential: lowest overpotential can be obtained at 10 mV/s (Figure 7a). Figure 7b shows the CV curves of the EOR upon changing the mass of the deposited catalyst (volume of the catalyst ink). Lowest overpotential (-31 mV) and highest mass activity were obtained for the lowest catalyst volume (1 µL, equals to 0.074 mg cm^{-2} catalyst load). Nanorod@ITO electrode possesses much lower mass activity in the supporting electrolyte (1 M KOH) in the absence of EtOH (Figure 7c). Similarly to the p-nitrophenol conversion and methylene blue degradation, the particles retain their original morphology and porosity after 30 CV cycles for EOR (Figure 7d). Porosity and multielemental nature of the tetrametallic nanorods significantly enhanced the EOR performance compared to the monometallic AuNRs.[58]

3. Conclusion

Unique tetrametallic nanorods were obtained by coating Au nanorods with a trimetallic (Pd, Pt, Ir) shell in a reliable and highly reproducible manner. The high porosity (micro- and mesoporosity) trimetallic shell was deposited onto the anisometric gold nanoparticles in a two-step protocol to ensure the sufficient reduction of Ir domains on the outer region of the PdPt shell. Beside the small size of the Pd and Pt nanograins in the shell, the presence of Ir further extends the application potential of the tetrametallic nanorods with active and available surface sites. In depth structural and elemental composition analyses revealed that the metals are located as well-defined layers around the Au nanorods: a porous Pd shell covers the nanorods followed by the thicker but also porous Pt layer decorated with

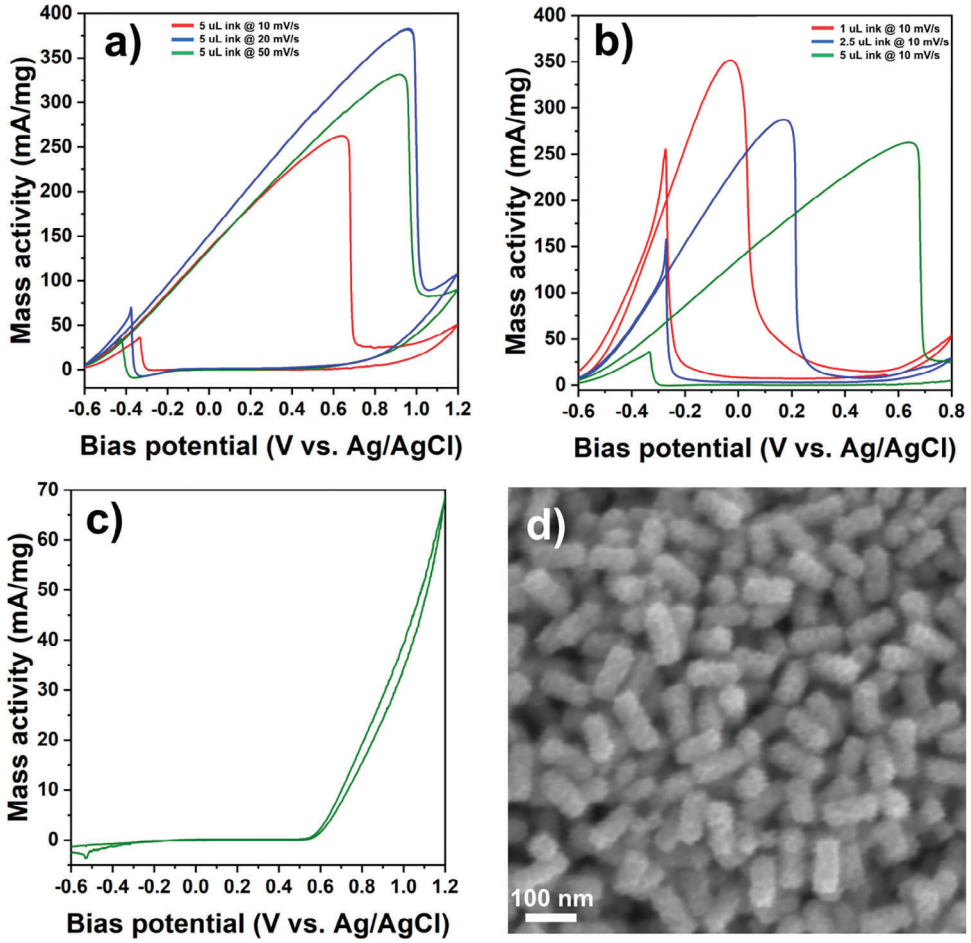

Figure 7. Voltammograms of ethanol oxidation reaction in the function of the scan rate a) and catalyst ink volume b). Mass activity of the nanorod@ITO electrode in 1 M KOH c). SEM image of the nanorod coating on ITO(MPTMS) after the ethanol oxidation reaction d). EOR (a) was performed in 1 M KOH as supporting electrolyte in the presence of EtOH (1 M).

Ir domains. Outstanding shape and size purity was achieved by revealing the impact of HCl and temperature on the precursors' stability and the micelle size of the pore forming copolymer (Pluronic F127). The porous tetrametallic nanorods possess high negative electrophoretic mobility, which is preserved even upon extensive washing, thus, this property is attributed to the electronic coupling of the metals and the consequent charge transfer towards the shell's surface. Multifunctionality of the nanocatalyst is demonstrated in various catalytic reactions: (i) the particles are able to convert p-nitrophenol to p-aminophenol with high rate, (ii) degradation of methylene blue takes place in the presence of particles without using external trigger (light, heat) which is attributed to the formation of OH radicals, (iii) ethanol can be electrocatalytically oxidized in alkaline medium with negative overpotential by the ITO-supported tetrametallic nanorods. It has to be emphasized that the shape and fine-structure of the catalyst nanorods are preserved in all catalytic test reactions demonstrating the robustness of the nanostructured particles. Multielemental synergy emerging in the tetrametallic nanorods allows the preparation of a functional nanomaterial with extendable potential in further catalytic purposes due to their unique structure and composition.

4. Experimental Section

Chemicals: Hydrogen tetrachloroaurate ($HAuCl_4$, ≥99.9%, trace metals basis), potassium tetrachloroplatinate (K_2PtCl_6, 99.9%, trace metals basis), chloroplatinic acid hexahydrate (H_2PtCl_6, ACS Reagent, ≥37.5% Pt basis), sodium tetrachloropalladate (Na_2PdCl_4, ≥99.9%, trace metals basis), sodium hexachloroiridate (Na_3IrCl_6), silver nitrate ($AgNO_3$, 99.9999%, trace metals basis), Pluronic F-127 (BioReagent), L-ascorbic acid (AA, BioXtra, ≥99.0%), sodium borohydride ($NaBH_4$, ReagentPlus, 99%), potassium hydroxide (KOH, ACS Reagent, ≥85%), methylene blue hydrate (MB, purum p.a., ≥97%), p-benzoquinone (p-BQ, ReagentPlus, ≥98%), sodium sulfite (Na_2SO_3, ACS Reagent, ≥98%), hydrochloric acid (HCl, puriss p.a., ACS Reagent, ≥37%), nitric acid (HNO_3, puriss p.a., ≥65%), Nafion perfluorinated resin solution (5 wt% in mixture of lower aliphatic alcohols and water, 45% water) were purchased from Merck (Sigma-Aldrich). Cetyltrimethylammonium bromide (CTAB, 99+%) and 4-nitrophenol (p-NP, 99%) were purchased from Thermo Scientific. Sodium oleate (NaOL, >97%) was acquired from TCI Chemicals. Ethanol (absolute, Normapure) and 2-propanol (Normapure) were supplied by VWR International. Ultrapure water (>18.2 MΩcm) was produced by a Sartorius Arium Mini. All glasswares and stirring bars were cleaned with *aqua regia* (3:1 V/V ratio of cc. HCl and HNO_3), rinsed thoroughly with ultrapure water, and dried at 70 °C. Quartz cuvettes were stored in 2 V/V% Hellmanex® II solutions, rinsed with ultrapure water and 2-propanol followed by drying under N_2 flow. All metal precursors, NaOL

and $NaBH_4$ were stored in a glove-box and their solutions were prepared freshly.

Synthesis of Gold Nanorods: Gold nanorods were synthesized based on the protocol of Ye et al.[44] In a 500 mL Schott glass, 9.0 g CTAB, 1.543 g sodium oleate and 250 mL MilliQ were mixed and stirred at 60 °C until the powders dissolved (30–40 minutes). After letting the solution cool down to room temperature, 18 mL $AgNO_3$ solution (4 mM) was added and the solution was gently stirred for 15 minutes followed by the addition of 250 mL $HAuCl_4$ solution (1 mM). After stirring for 90 minutes, the yellowish growth solution turned colorless.

In this time window, the seed solution was prepared by swiftly injecting 0.5 mL ice-cold $NaBH_4$ solution (0.006 M) into the vigorously stirred mixture of 2.5 mL CTAB solution (0.2 M) and 2.5 mL $HAuCl_4$ solution (0.5 mM). The seed solution was stirred for 2 minutes and then left undisturbed for 30 minutes.

To the previously prepared growth solution, 2.1 mL cc. HCl was added and the solution was further stirred for 15 minutes. Then 1.25 mL ascorbic acid solution (0.064 M) was added followed by the rapid injection of the seeds (400 µL). The solution was vigorously stirred for 1–2 minutes, the stirring bar was removed and the growth solution was left undisturbed overnight in a temperature-controlled bath at 28 °C to avoid the crystallization of CTAB. Purification and concentration of the gold nanorod solution was performed via centrifuging the redispersion in 50 mL Falcon tubes (6500 rcf, 20 min) and the precipitate was redispersed in a total of 14 mL CTAB solution (50 mM). This step was crucial for extending the shelf life and retaining the morphology of the nanorods via suppressing the concentration of the unreacted reactants and it eases the further concentration of the nanorods for the mesoporous multimetallic shell growth. The Au concentration of this AuNR stock solution was calculated based on the extinction value at 400 nm[59] and was found to be 8.91 mM.

Synthesis of Tetrametallic Nanorods: Tetrametallic mesoporous NRs were synthesized by simplifying, optimizing and extending the protocol of Deng et al.[21] to perform a two-step growth of the trimetallic shell around the AuNRs. AuNR stock solution (1.346 mL) was centrifuged in an Eppendorf tube, the supernatant was removed and the NRs were redispersed in 1 mL F127 solution (3 wt%). To further suppress the CTAB concentration and increase the concentration of the AuNRs, this solution was centrifuged once more at the same conditions. After removing the supernatant, 50 µL F127 solution (3 wt%) was added and the particles were redispersed using vortexing and ultrasonication. In a 40 mL vial, 1.419 mL MilliQ, 0.501 mL F127 solution (10 wt%) and 60 µL HCl solution (6 M) were mixed and heated to 70 °C in an aluminum heat block. Afterwards, 120 µL Na_2PdCl_4 (100 mM), 120 µL K_2PtCl_4 (100 mM), 180 µL H_2PtCl_6 (100 mM) solutions were sequentially added under stirring at 70 °C. To this solution, the previously prepared AuNR solution (50 µL) was injected. To initiate the shell growth, 3 mL ascorbic acid solution (100 mM, preheated to 70 °C) was added under vigorous stirring and the solution was stirred for 40 minutes at 70 °C (the concentration of Au^0 was 2.2 mM at this stage). Afterwards, the temperature was increased to 80 °C and 60 µL Na_3IrCl_6 solution (100 mM), 807 µL ascorbic acid (100 mM, preheated to 80 °C) was added. To quickly reduce the Ir^{3+}, 284 µL $NaBH_4$ solution (25 mg/mL in room temperature MilliQ) was swiftly added under stirring. The solution was kept at 80 °C for an additional 20 minutes. After naturally cooling to room temperature, the black solution was diluted to 60 mL with F127 solution (0.05 wt%) and centrifuged at 1500 rcf for 15 min in 3×20 mL portions. The slightly colored supernatant was removed and 15 mL MilliQ was added to each centrifuge tube. In a second centrifugation step (5000 rcf, 15 min), the supernatant was removed and the mesoporous nanorods were redispersed in a total of 2.25 mL MilliQ. This solution is referred to as the "stock solution" and has a total metal concentration of 1.991 g L^{-1} (measured by ICP-OES).

Optical Characterization: Stock solution of tetrametallic nanorods was diluted with a factor of 100 with MilliQ water in QS quartz cuvette. The extinction spectrum of the particles was recorded in a Shimadzu UV 3600i UV-Vis-NIR spectrophotometer in the wavelength range of 200–1400 nm. Absorption spectrum of the tetrametallic nanorods was measured in an integrating sphere of an Edinburgh FS-5 spectrofluorometer.

Electron Microscopy: Nanoparticles were deposited from their diluted stock solution onto Si wafers or carbon-coated Cu grids for SEM and TEM investigations, respectively (via drop casting 1 µL of solution and drying at ambient conditions). A Zeiss LEO 1540-XB was used to take the SEM images at an accelerating voltage of 5 keV. Elemental composition of the samples was investigated by energy dispersive X-ray spectroscopy using an Oxford Instruments UltimMax 40 detector. TEM, STEM images and STEM-EDX maps were recorded using a ThermoFischer THEMIS 200 transmission electron microscope operated at 200 kV equipped with spherical aberration corrected objective lens and Bruker SuperX X-ray detectors and with a JEOL 3010 microscope operated at 300 kV. STEM elemental maps presented in this paper show net intensities after background subtraction and peak deconvolution as evaluated by the Velox software.

XRD and XPS Sample Preparation and Measurements: Stock solution of the nanoparticles was concentrated with a factor of 20, drop-cast and dried onto Si wafer. XRD diffractograms were taken with a Bruker AXS D8 Discover X-ray diffractometer equipped with Göbel-mirror and scintillation detector using Cu Kα ($\lambda = 1.5406$ Å) radiation. The X-ray beam dimensions were 1 mm × 5 mm, the 2Θ step size was 0.05°, scan speed 0.15° min^{-1}. The Diffrac.EVA program and the ICDD PDF database was used for phase identification. A ThermoFischer Escalab Xi+ instrument was used for the XPS measurements equipped with an Al Kα source focused onto an area of 0.5 mm in diameter. Optical image as well as XPS identification supported the selection of areas with high particle coverage. Spectra were recorded with energy resolution of 0.6 eV and 0.1 eV step size with 0.5 s per point speed. Binding energy scale was adjusted using the adventitious carbon peak fixed at 284.6 eV.

Electrophoretic Mobility: A Malvern ZetaSizer Nano ZS was used to perform dynamic light scattering (λ = 635 nm) measurements on the diluted aqueous solutions of the particles. Electrophoretic mobilities were determined in folded capillary cells (DTS-1070).

ICP-OES: A portion of the mesoporous nanorod stock solution (100 µL) was digested in *aqua regia* (675 µL cc. HCl + 225 uL cc. HNO_3) for 15 minutes. After the nanorods dissolved, the solution was topped up to 10 mL by adding 8.9 mL of MilliQ water and 100 µL Y standard solution (100 ppm Y in 2% HNO_3). Concentration of the metals were determined by a Perkin Elmer Avio 200 ICP-OES instrument by considering the wavelength of 242.795 nm for Au, 340.458 nm and 324.458 nm for Pt, 214.423 nm and 265.945 nm for Pd and 224.268 nm and 215.268 nm for Ir to avoid spectral overlapping.

Conversion of p-nitrophenol to p-aminophenol: in a semi-micro quartz cuvette, MilliQ water, p-nitrophenol stock solution (0.012 M), $NaBH_4$ (0.1 M prepared with ice-cold MilliQ) and the porous nanorod stock solution were sequentially added. For experiments at 0.08 mM p-nitrophenol concentration, 993 µL MilliQ, 6.67 µL 0.012 M p-nitrophenol solution, 3.33 µL 0.1 M $NaBH_4$ and 3 µL nanorod stock solution was used. For experiments at 0.16 mM p-nitrophenol concentration, 987 µL MilliQ, 13.33 µL 0.012 M p-nitrophenol solution, 6.66 µL 0.1 M $NaBH_4$ and 6 µL nanorod stock solution was used. After adding the NRs, the time-dependent UV–vis spectra were taken in a Shimadzu UV3600i spectrophotometer with a time resolution of 46.45 s for each step for 1 hour.

Degradation of Methylene Blue: A methylene blue stock solution having a concentration of 100 mg L^{-1} was prepared. For a typical experiment, 980 µL of MilliQ water was added into a PMMA semi-micro cuvette followed by the addition of 15 µL mNR stock solution. This solution was measured as a reference before adding the methylene blue. Time-resolved visible spectra were taken with a fiber coupled Thorlabs CCS200 spectrometer after the addition of 20 µL methylene blue stock solution. The spectra were collected for 2 hours with a time resolution of 10 s. For $OH^{\cdot}$ radical scavenging, 930 µL MilliQ water and 50 µL 2-propanol were used by keeping the other parameters constant. For O_2 and $O_2^{\cdot -}$ scavenging, 980 µL MilliQ and 10 µL Na_2SO_3 solution (8 mM) or 10 µL p-benzoquinone (8 mM) were used, respectively. To suppress the concentration of the dissolved oxygen, the sample was bubbled with Ar for 15 minutes before the addition of the methylene blue. To reveal the effect of the illumination on the dye degradation kinetics, a lab-built 300 W Xe lamp was used to illuminate the sample (power density of ca. 970 µW cm^{-2}) and the spectra were taken after 5, 10, 20, 30, 60, 90, 120 minutes in the fiber-coupled spectrometer.

Preparation of the Nanorod-ITO Electrodes: ITO on glass (VisionTek, 12 Ω sq^{-1}) was cut into pieces with dimensions of 1.5 cm (width) and 3.0 cm (height). The substrates were successively ultrasonicated in acetone, 2-propanol and MilliQ water for 10-10 minutes. After rinsing with MilliQ water, the substrates were activated in NH_4OH:H_2O_2:MilliQ solution (consisting of 100 mL MilliQ, 9 mL 50% H_2O_2 and 13 mL 28–32% NH_4OH) at 70 °C for 2 hrs followed by excessive rinsing with MilliQ, 2-propanol and toluene and drying with a N_2 gun. The substrates (8-10 pieces) in a PTFE holder were immersed into the functionalization solution (100 mL of toluene + 2 mL MPTMS), the temperature was set to 70 °C and were gently stirred for 2 hrs on a hot plate. Afterwards, the heating was turned off and the solution was kept stirred overnight at room temperature. Evaporation of toluene was suppressed via covering the beaker with aluminum foil. Then, the substrates were rinsed with toluene and dried under N_2 flow followed by a thermal treatment (50 °C, 2 hrs) in a drying oven. After removing them from the oven, the substrates were stored in a N_2-filled glovebox (O_2 = 0.7 ppm, H_2O = 0.1 ppm). Before the preparation of the electrode, the ITO(MPTMS) slide was taken out of the glovebox and a mold was glued on its surface (prepared from scotch tape, 1.5×1.5 cm rectangle with a 0.5×0.5 cm rectangular opening in the middle). The catalyst ink was prepared by centrifuging 100 µL of the aqueous mNR stock solution at 3000 rcf for 5 min. Upon removing 95 µL supernatant, the particles were redispersed in water by adding 95 µL of fresh MilliQ water. In a second centrifugation step, 95 µL of supernatant was removed and 5 µL ethanol was added to the precipitate. After thorough ultrasonication and vortexing, 0.8 µL of Nafion solution was added to the ink followed by ultrasonication for 5 minutes. Ratio of Nafion:nanorods was chosen to avoid the block of interfacial mass transport and active sites.[60] From this ink solution, 1–5 µL was deposited into the mold's opening and let dry for 30 minutes at ambient conditions. After drying, the mold was gently removed by tweezers. Based on the elemental composition measured by ICP-OES, the catalyst ink volumes of 1, 2.5 and 5 µL represent 0.0737, 0.1844 and 0.3687 mg cm^{-2} catalyst loads in the mold (area = 0.25 cm^2) in terms of total metal loads, respectively.

Electrocatalytic Ethanol Oxidation Reactions: EOR experiments were carried out in a conventional three-electrode electrochemical setup consisting of an Ag/AgCl (3 M KCl, BASi) reference electrode, a Pt wire counter electrode (BASi) and the mNR@ITO(MPTMS) slide as working electrode. Ethanol was added to 1 M KOH solution to set the ethanol concentration to 1 M and the electrolyte was bubbled with Ar for 1 hour. Cyclic voltammetry measurements were performed by a Gamry Reference 3000 potentiostat in the bias potential range of −0.6 – 0.8 V or −0.6 – 1.2 V.

Statistical Analysis: particle size and pore size distributions were presented as mean ± standard deviation. Sample size was 200 for nanoparticles and pores as well. Normal distribution curves were applied to all histograms. Data visualization and statistical analysis was performed with OriginLab OriginPro 2021 (version 9.8). Image processing was carried out by using ImageJ.

Supporting Information

Supporting Information is available from the Wiley Online Library or from the author.

Acknowledgements

The authors thank Apoko Stephen Omondi for his assistance in the nanorod preparation. D.K. acknowledges the support of Pro Progressio and József Varga Foundation. The work was financially supported by the NRDI fund of Hungary under the grant of FK 142148. Project no. TKP2021-NKTA-05 has been implemented with the support provided by the Ministry of Innovation and Technology of Hungary from the National Research, Development and Innovation Fund (NRDI), financed under the TKP2021 funding scheme. The authors thank the support of VEKOP-2.3.3-15-2016-00002 of the European Structural and Investment Funds.

Conflict of Interest

The authors declare no conflict of interest.

Data Availability Statement

The data that support the findings of this study are available from the corresponding author upon reasonable request.

Keywords

(electro)catalysis, ethanol oxidation reaction, mesoporous tetrametallic nanorods, multielemental synergy, multimetallic nanorods

Received: January 18, 2024
Revised: February 12, 2024
Published online:

[1] T. S. Rodrigues, A. G. M. da Silva, P. H. C. Camargo, *J. Mater. Chem. A* **2019**, *7*, 5857.
[2] Y. Shi, Z. Lyu, M. Zhao, R. Chen, Q. N. Nguyen, Y. Xia, *Chem. Rev.* **2021**, *121*, 649.
[3] J. N. Hansen, H. Prats, K. K. Toudahl, N. Mørch Secher, K. Chassn, J. Kibsgaard, *ACS Energy Lett.* **2021**, *6*, 1175.
[4] G. Xu, L. Yang, J. Li, C. Liu, W. Xing, J. Zhu, *Adv. Sens. Energy Mater.* **2023**, *2*, 100058.
[5] K. D. Gilroy, A. Ruditskiy, H.-C. Peng, D. Qin, Y. Xia, *Chem. Rev.* **2016**, *116*, 10414.
[6] M. Zhou, C. Li, J. Fang, *Chem. Rev.* **2021**, *121*, 736.
[7] W. He, X. Han, H. Jia, J. Cai, Y. Zhou, Z. Zheng, *Sci. Rep.* **2017**, *7*, 40103.
[8] X. Zhu, Q. Guo, Y. Sun, S. Chen, J.-Q. Wang, M. Wu, W. Fu, Y. Tang, X. Duan, D. Chen, Y. Wan, *Nat Commun.* **2019**, *10*, 1428.
[9] K. Jukk, N. Kongi, K. Tammeveski, J. Solla-Gullón, J. M. Feliu, *Electrochem. Commun.* **2015**, *56*, 11.
[10] J. Zhang, L. Wan, L. Liu, Y. Deng, C. Zhong, W. Hu, *Nanoscale* **2016**, *8*, 3962.
[11] A. K. Taylor, D. S. Perez, X. Zhang, B. K. Pilapil, M. H. Engelhard, B. D. Gates, D. A. B. Rider, *J. Mater. Chem. A* **2017**, *5*, 21514.
[12] S. W. Kang, Y. W. Lee, Y. Park, B.-S. Choi, J. W. Hong, K.-H. Park, S. W. Han, *ACS Nano* **2013**, *7*, 7945.
[13] S. Liu, S. Yin, H. Zhang, S. Jiao, Z. Wang, Y. Xu, X. Li, L. Wang, H. Wang, *Chem. Eng. J.* **2022**, *428*, 131070.
[14] Y. Zheng, Y. Ma, G. Zhang, W. Zhao, F. Liu, M. Liu, *CrystEngComm* **2021**, *23*, 6879.
[15] L. D. Germano, V. S. Marangoni, N. V. V. Mogili, L. Seixas, C. M. U. Maroneze, *ACS Appl. Mater. Interfaces* **2019**, *11*, 5661.
[16] H. Lv, Y. Wang, L. Sun, Y. Yamauchi, B. Liu, *Nat. Protoc.* **2023**, *18*, 3126.
[17] X. Min, H. Lv, Y. Yamauchi, B. Liu, *CCS Chem.* **2022**, *4*, 1829.
[18] Y. H. Ahmad, A. T. Mohamed, A. Alashraf, M. Matalqeh, A. El-Shafei, S. Y. Al-Qaradawi, A. S. Aljaber, *Appl. Surf. Sci.* **2020**, *508*, 145222.
[19] Y. Kang, O. Cretu, J. Kikkawa, K. Kimoto, H. Nara, A. S. Nugraha, H. Kawamoto, M. Eguchi, T. Liao, Z. Sun, T. Asahi, Y. Yamauchi, *Nat. Commun.* **2023**, *14*, 4182.
[20] H. Lv, D. Xu, L. Sun, J. Henzie, A. Lopes, Q. Gu, Y. Yamauchi, B. Liu, *Nano Lett.* **2019**, *19*, 3379.
[21] Y. Deng, H. Xue, S. Lu, Y. Song, X. Cao, L. Wang, H. Wang, Y. Zhao, H. Gu, *ACS Appl. Energy Mater.* **2018**, *1*, 4891.
[22] Y. Pan, J. Gao, Y. Li, E. Lv, U. Khan, X. Yang, J. Yao, A. Nairan, Q. Zhang, *Small* **2024**, *20*, 2304594.

[23] Y. Pan, J. Gao, E. Lv, T. Li, H. Xu, L. Sun, A. Nairan, Q. Zhang, *Adv Funct. Mater.* **2023**, *33*, 2303833.
[24] Y. Wang, L. Sun, H. Lv, C. Zheng, B. Liu, *CCS Chem.* **2023**, *5*, 1896.
[25] L. Wang, Y. Yamauchi, *J. Am. Chem. Soc.* **2010**, *132*, 13636.
[26] B. Jiang, H. Ataee-Esfahani, C. Li, S. M. Alshehri, T. Ahamad, J. Henzie, Y. Yamauchi, *Chem. A Eur. J.* **2016**, *22*, 7174.
[27] M. T. Gorzkowski, A. Lewera, *J. Phys. Chem. C* **2015**, *119*, 18389.
[28] G. Zhi, X. Zhang, W. Qiao, L. Feng, *Energy Fuels* **2023**, *37*, 2359.
[29] S.-H. Chang, M.-H. Yeh, J. Rick, W.-N. Su, D.-G. Liu, J.-F. Lee, C.-C. Liu, B.-J. Hwang, *Sens. Actu. B: Chem.* **2014**, *190*, 55.
[30] H. L. K. S. Stolle, J. J. Kluitmann, A. Csáki, J. M. Köhler, W. Fritzsche, *Catalysts* **2021**, *11*, 1442.
[31] H. Lee, S. E. Habas, G. A. Somorjai, P. Yang, *J. Am. Chem. Soc.* **2008**, *130*, 5406.
[32] H. Zhang, M. Jin, Y. Xia, *Chem. Soc. Rev.* **2012**, *41*, 8035.
[33] M. Hosseini, T. Barakat, R. Cousin, A. Aboukaïs, B.-L. Su, G. De Weireld, S. Siffert, *Appl. Catal. B: Environ.* **2012**, *111*, 218.
[34] Q. Wang, G. Hong, Y. Liu, J. Hao, S. Liu, *RSC Adv.* **2020**, *10*, 25209.
[35] M. Cui, X. Huang, X. Zhang, Q. Xie, D. Yang, *New J. Chem.* **2020**, *44*, 18274.
[36] P. Peljo, J. A. Manzanares, H. H. Girault, *Langmuir* **2016**, *32*, 5765.
[37] B. P. Williams, M. Yaguchi, W.-S. Lo, C.-R. Kao, L. K. Lamontagne, B. T. Sneed, C. N. Brodsky, L.-Y. Chou, C.-H. Kuo, C.-K. Tsung, *Nanoscale* **2020**, *12*, 8687.
[38] M. Chen, D. Kumar, C.-W. Yi, D. W. Goodman, *Science* **2005**, *310*, 291.
[39] A. E. Baber, H. L. Tierney, E. C. H. Sykes, *ACS Nano* **2010**, *4*, 1637.
[40] C. Hu, Y. Zhou, M. Xiao, G. Yu, *Int. J. Hydrogen Energy* **2020**, *45*, 4341.
[41] F. J. Perez-Alonso, D. N. McCarthy, A. Nierhoff, P. Hernandez-Fernandez, C. Strebel, I. E. L. Stephens, J. H. Nielsen, I. Chorkendorff, *Angew. Chem., Int. Ed.* **2012**, *51*, 4641.
[42] K. Yamamoto, T. Imaoka, W.-J. Chun, O. Enoki, H. Katoh, M. Takenaga, A. Sonoi, *Nat. Chem.* **2009**, *1*, 397.
[43] W. Ji, W. Qi, S. Tang, H. Peng, S. Li, *Nanomaterials* **2015**, *5*, 2203.
[44] X. Ye, C. Zheng, J. Chen, Y. Gao, C. B. Murray, *Nano Lett.* **2013**, *13*, 765.
[45] P. J. Mayne, *Polyhedron* **1984**, *3*, 1013
[46] D. Liu, S. Lu, Y. Xue, Z. Guan, J. Fang, W. Zhu, Z. Zhuang, *Nano Energy* **2019**, *59*, 26.
[47] P. Lettenmeier, J. Majchel, L. Wang, V. A. Saveleva, S. Zafeiratos, E. R. Savinova, J.-J. Gallet, F. Bournel, A. S. Gago, K. A. Friedrich, *Chem. Sci.* **2018**, *9*, 3570.
[48] B. Ballinger, J. Motuzas, S. Smart, S. Ismail, N. A. Zubir, S. Nurehan, A. Jalil, J. C. D. Da Costa, *J. Sol-Gel Sci. Technol.* **2020**, *95*, 456.
[49] L. I. Elding Palladium(U) Halide Complexes. I. Stabilities and Spectra of Palladium(I1) Chloro and Bromo Aqua Complexes.
[50] M. Sokolsky-Papkov, A. Kabanov, *Polymers* **2019**, *11*, 1553.
[51] J. Strachan, C. Barnett, A. F. Masters, T. Maschmeyer, *ACS Catal.* **2020**, *10*, 5516.
[52] Y.-Q. Dou, Q. Zhang, T.-S. Deng, Z. Cheng, X. Zhao, *J. Mater. Sci.* **2024**, *59*, 2302.
[53] A. A. Alshehri, M. A. Malik, *Catalysts* **2020**, *10*, 1138.
[54] S. R. Georgescu, C. I. Mitran, M. I. Mitran, I. Nicolae, C. Matei, C. D. Ene, G. L. Popa, M. Tampa, *JCM* **2021**, *10*, 2692.
[55] T. Zhang, T. Oyama, A. Aoshima, H. Hidaka, J. Zhao, N. Serpone, *J. Photochem. Photobiol. A: Chem.* **2001**, *140*, 163.
[56] I. Khan, K. Saeed, I. Zekker, B. Zhang, A. H. Hendi, A. Ahmad, S. Ahmad, N. Zada, H. Ahmad, L. A. Shah, T. Shah, I. Khan, *Water* **2022**, *14*, 242.
[57] Y. Zhao, X. Li, J. M. Schechter, Y. Yang, *RSC Adv.* **2016**, *6*, 5384.
[58] D. Zámbó, P. Rusch, F. Lübkemann, N. C. Bigall, *ACS Appl. Mater. Interfaces* **2021**, *13*, 57774.
[59] L. Scarabelli, A. Sánchez-Iglesias, J. Pérez-Juste, L. M. Liz-Marzán, *J. Phys. Chem. Lett.* **2015**, *6*, 4270.
[60] G.-F. Li, D. Yang, P.-Y. Abel Chuang, *ACS Catal.* **2018**, *8*, 11688.